

Quantitative analysis of relative geolocation accuracy of the TerraSAR-X enhanced ellipsoid corrected product

Takashi Nonaka,^{a,*} Tomohito Asaka,^a Keishi Iwashita,^a Wen Liu,^b
Fumio Yamazaki,^b and Tadashi Sasagawa^c

^aNihon University, College of Industrial Technology, Chiba, Japan

^bChiba University, Department of Urban Environment Systems, Chiba, Japan

^cPasco Corporation, Tokyo, Japan

Abstract. High-resolution commercial synthetic aperture radar (SAR) satellites with resolutions of several meters have recently been used for effective disaster monitoring. One study reported the earthquake's displacement using the pixel matching method with both pre- and postevent TerraSAR-X data, with a validated accuracy of ~30 cm at global navigation satellite system (GNSS) Earth observation network (GEONET) reference points. However, it is insufficient to determine the accuracy using analysis of only a couple of data points per orbit. In addition, the errors were not reported because the number of data samples was too small to discuss the statistics. In order to better understand displacement accuracy, we analyzed displacement features using the pixel matching method to evaluate the relative geolocation accuracies of the TerraSAR-X product. First, we used fast Fourier transform oversampling 16 times to develop the pixel matching method for estimating the displacement at the subpixel level using the TerraSAR-X StripMap dataset. Second, we applied this methodology to 20 pairs of images from the Tokyo metropolitan area and calculated the displacement for each image pair. Third, we conducted spatial and temporal analyses in order to understand the displacement features. Finally, we evaluated the displacement accuracy by comparison with GEONET and solid earth tide data as a reference. © 2017 Society of Photo-Optical Instrumentation Engineers (SPIE) [DOI: 10.1117/1.JRS.11.044001]

Keywords: displacement; geometric feature; pixel matching; time series analysis; synthetic aperture radar.

Paper 170229 received Mar. 16, 2017; accepted for publication Sep. 6, 2017; published online Oct. 4, 2017.

1 Introduction

Commercial high-resolution synthetic aperture radar (SAR) satellites, with resolutions of several meters, have been in operation for the past few years; a variety of information is available depending on sensor specifications. For example, sensors for various wavelengths include TerraSAR-X (X-band SAR with 3.1-cm wavelength), Radarsat-2 (C-band SAR with 5.6-cm wavelength), and ALOS PALSAR-2 (L-band SAR with 23.6-cm wavelength). SAR data have widespread applications, including stability analysis of individual structures,¹ mining applications,² subsidence monitoring,³ and forest mapping;⁴ disaster monitoring is another useful potential application area. For instance, many researchers used SAR data to study the large earthquake that occurred off the coast of the Tohoku region of Japan on March 11, 2011 [also known as the great Japan earthquake, (GJE)]; these studies estimated the flooded area,⁵ building damage,⁶ and ground displacement.⁷

Interferometric synthetic-aperture radar (InSAR) is a well-established technique for estimating centimeter-scale displacement using differences in return-wave phase,⁸ although the results can be ambiguous when the displacement gradient exceeds half a fringe per pixel. Furthermore, InSAR may not always be able to observe deformation, if vegetation or temporal factors lead to

*Address all correspondence to: Takashi Nonaka, E-mail: nonaka.takashi@nihon-u.ac.jp

a lack of correlation between pixels. Moreover, measured displacement provides only one component of the vector [slant range (SR) direction]. Pixel matching, on the other hand, models the displacement field by translation derived from the local cross-correlation peaks, and is an alternative for estimating displacement on the subpixel to pixel scale using intensity information.

In previous studies, we evaluated displacements from the GJE using pairs of pre- and post-event SAR images⁹ and proposed a methodology for detecting three-dimensional (3-D) displacements using several pairs of TerraSAR-X intensity images acquired from different orbits.¹⁰ This method measures the displacement of nondamaged buildings with strong radar backscatter; we measured several meters of displacement with an accuracy of ~30 cm. However, when evaluating the relative geolocation accuracy of SAR data, it is necessary to consider the output's spatial variation; this may require the temporal analysis of dozens of image pairs. One recent study determined that the absolute geometric accuracy of TerraSAR-X is less than 10 cm,¹¹ while another revealed the absolute geolocation accuracy of the TerraSAR-X ortho-rectified enhanced ellipsoid corrected (EEC) product in both flat and mountainous areas using the difference method, though the relative accuracy was not included.¹² Our study evaluated the relative two-dimensional (2-D) geolocation pointing accuracy of TerraSAR-X using 21 images with the same acquisition conditions, revealing the geolocation features of both spatial and temporal variation.

2 Data and Study Site

2.1 Data

2.1.1 TerraSAR-X

TerraSAR-X and TanDEM-X are the German radar satellites launched in June 2007 and June 2010, respectively. Both carry X-band (9.65 GHz) SAR sensors and operate in several different imaging modes:¹³ the 300-MHz high-resolution staring spotlight mode achieves a spatial resolution of 25 cm (azimuth), the StripMap and ScanSAR modes allow acquisition with resolutions of 3 and 18 m, respectively, and the Wide ScanSAR mode covers a swath width of 200 to 270 km, depending on the incidence angle. One mission of these satellites is to produce a global digital elevation model (DEM) with an absolute height error of 10 m and a relative height error of 2 m.¹⁴ We acquired a series of TerraSAR-X images with the acquisition parameters shown in Table 1. The EEC product was used in this study because it features the highest level of geometric correction available for TerraSAR-X basic image products and is widely used due to being quickly interpretable and combinable with other sources of information. We corrected image distortion of the EEC product using a DEM generated by the geospatial information authority (GSI) of Japan¹⁵ and projected the product with a resampled square pixel size of 1.25 m. Although a previous study had shown that DEM errors could affect the absolute geolocation accuracy,¹⁶ such errors were discarded in our time series analysis as all images had the same incidence angle.

2.1.2 GNSS Earth Observation Network System Data

GSI has established ~1200 Global Positioning System (GPS) ground control stations throughout Japan, called the global navigation satellite system (GNSS) Earth observation network system (GEONET). Real-time observation of crustal displacement is made possible by continuous observations at the stations, where radio waves from the GPS satellites are constantly received; ground displacement has been monitored by GEONET since 1993.¹⁷ Although GEONET is one of the densest GPS networks in the world, the distance between neighboring stations is greater than 20 km. For example, Fig. 1 shows the absolute displacement observed by the GEONET ground station shown in Fig. 2, relative to a June 22, 2010, reference date. Each point corresponds to an acquisition date of TerraSAR-X data. The measured displacement was almost 0 cm before the end of 2010, but 1 cm of western displacement was observed on January 6, 2011, and more than 20 cm of eastern and 5 cm of northern displacement was observed on March 13, 2011,

Table 1 Acquisition parameters of TerraSAR-X imagery.

Acquisition mode	StripMap		
Product type	EEC		
Resolution	3 m		
Pixel spacing	1.25 m		
Polarization	HH		
Incidence angle	42.8 deg		
Inclination	97.44 deg		
Acquisition time	5:43 (JST)		
Acquisition date	Year	Month	Date
	2010	June	22
		July	3, 14
		August	16, 27
		September	7, 18
		November	1, 23
		December	15, 26
	2011	January	6, 17
		March	2, 13, 24
		July	12, 23
		August	3, 25
		September	5

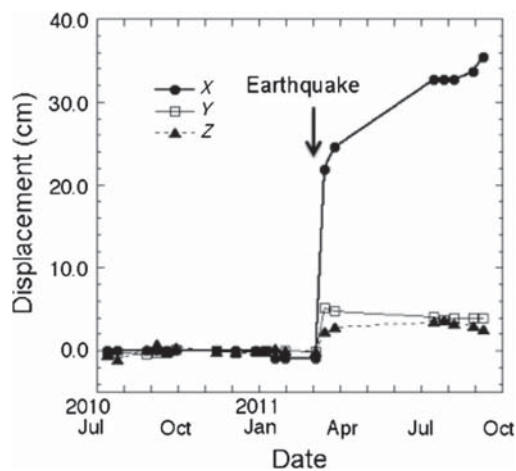


Fig. 1 Absolute displacement relative to a June 22, 2010, reference date, observed at the GEONET ground station shown in Fig. 2. The points from July 3, 2010, to September 5, 2011, correspond to the acquisition dates of TerraSAR-X data.

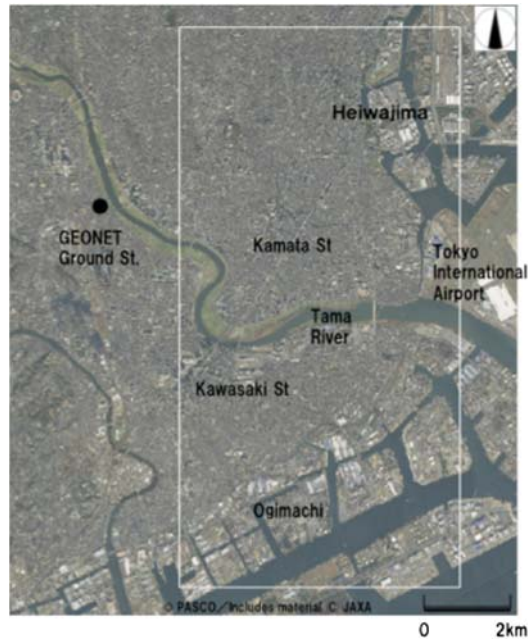


Fig. 2 Study area of Tokyo Ota-ku and Kawasaki-shi in Kanagawa Prefecture, including the location of the GEONET ground station used. White box is 6 km \times 12 km.

just after the GJE. Even after the earthquake, more than 10 cm of continuous eastward displacement was observed for an additional six months.

2.2 Study Site

Figure 2 shows the study site located around Tokyo Ota-ku and Kawasaki-shi in the Kanagawa Prefecture region; the white frame shows the analyzed area. The Tama River flows from west to east through the center of the study site; the north side of the river is Tokyo-to and the south side is Kanagawa Prefecture. The site mainly consists of densely built-up areas, with many sources of strong scattering, which is important for our methods. The buildings, both residential and industrial, are very crowded and include the Kamata and Kawasaki railway stations. The Kawasaki GEONET ground station used in this study is about several kilometers west of the study area.

3 Methodology

We estimated the subpixel-level displacement using the pixel matching method, which is an image processing technique used to estimate displacement in both X - and Y -directions. This study excludes Z -direction due to the effects being little.¹⁸ The general pixel matching method¹⁹ was customized for analyzing TerraSAR-X images (Fig. 3).

We first applied cross correlation on 200 subareas distributed over the image (Fig. 4) and automatically selected the pixel with maximum intensity to extract the manmade objects for each subarea from the master image. We then clipped a certain window size (with the maximum intensity pixel at the center) and found that the matching points of corresponding slave images had the maximum correlation coefficients. The adoption of a large correlation window size (128 \times 128 pixels) decreased the amount of poor offset data.

Next, we estimated the offset at the subpixel level by calculating the square of DN values for 8 \times 8 pixels (both master and slave images) and clipping with the representative pixel of each subarea located at the center of each correlation window. Then, we applied fast Fourier transform oversampling 16 times to estimate the displacement of subpixel resolution for each subarea. Finally, we produced maps of X - and Y -displacements for the entire image, which we combined

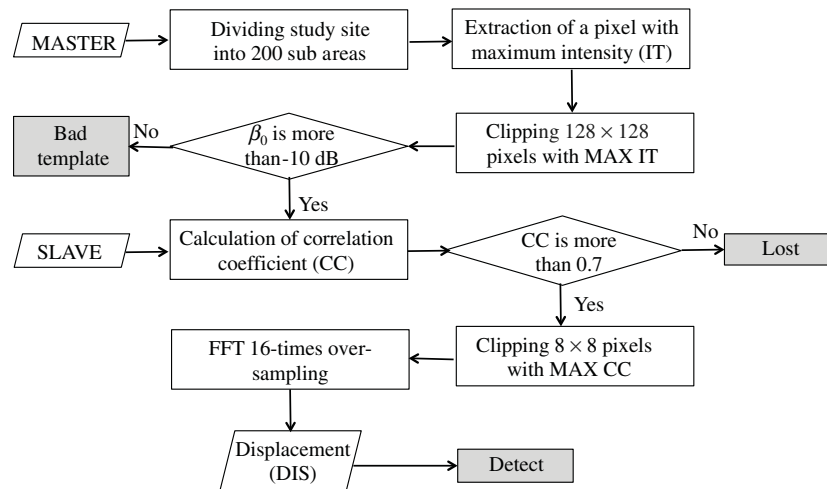


Fig. 3 Pixel matching procedure for estimating the displacement at the subpixel scale from a pair of TerraSAR-X images.

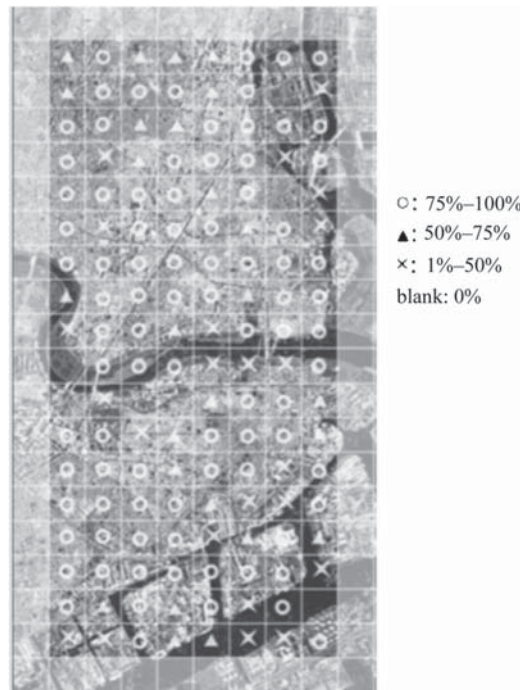


Fig. 4 Division of 200 subareas in the study site. Symbols show the “detect” ratio (sufficient radar brightness) for 20 pairs of data in each subarea.

with that of each subarea. In order to minimize mismatching, we used an optimized threshold value for maximum intensity, correlation coefficient, and displacement.²⁰

4 Results

4.1 Classification of Image Status

Using pairs of master and slave images, we fixed the master to the data acquired on June 22, 2010, and the slaves to the other images. Using a pixel size of 1.25 m in the standard StripMap mode provided a minimum detectable offset (MDO) of 0.0625 (1/16) pixels (corresponding to

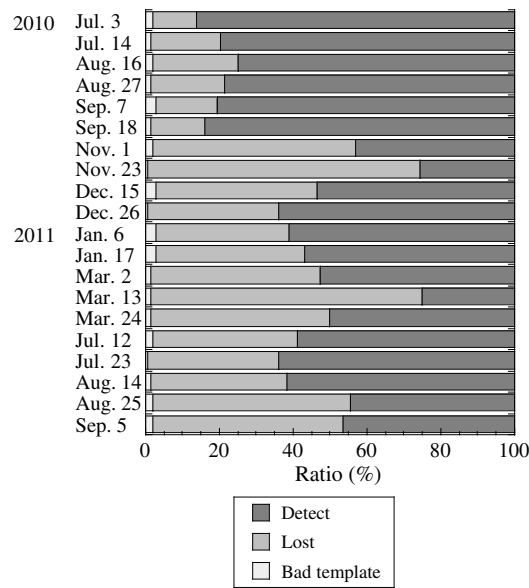


Fig. 5 Ratio of data categories for the each TerraSAR-X master-slave image pair; vertical axis is acquisition date of slave image.

about 7.8 cm for the TerraSAR-X image with 1.25 m pixel spacing). We also divided the matching status into three categories: “detect,” “lost,” and “bad template.”²¹ The study area consists of many sources of strong scattering, however, Tama River and riverside grass were included in the study site. To remove the pixels of these natural objects, if average radar brightness (β_0) values inside a window size of data were less than -10 dB, we discarded the data as “bad template.” For the remaining data, the threshold of the correlation coefficients is necessary to discard the changed man-made objects. In the previous study, the TerraSAR-X StripMap images were utilized for the Sendai region, more than 80% of the correlation coefficients were less than 0.70 for the damaged buildings, while about 85% were more than 0.70 for the nondamaged buildings.²² Thus, if the correlation coefficient was less than 0.70, they were regarded as “lost;” data that passed these tests were classified as “detect.”

Figure 5 shows the ratio of the three categories for each pair of images. Several subareas, including the Tama River, were classified as “lost” for most pairs (Fig. 4). The detection rate (defined as the ratio of “detect”) for most of the pairs was more than 50% and was more than 80% when the image pair had a time interval of less than 3 months. Figure 5 clearly shows that the detection rate was less than 30% for the image pair acquired just after the GJE (March 13, 2011); however, the detection rate had recovered by acquisition of the next image pair. The detection rate on November 23, 2010 was also low, at less than 30% (though the cause is not clear). Therefore, these two data sets were excluded from the analysis.

4.2 Spatial Features of the Displacement

Estimated displacement generally shows spatial variations, and it is important to consider whether this variation is significant or not. Therefore, we evaluated the relative geolocation accuracy from the spatial distribution of the displacement for each image pair. The displacement value was derived from the pixels classified as “detect.” The average spatial distribution in the X- and Y-directions was 10 and 4.5 cm, respectively, while the standard deviation as 1.8 and 0.6 cm, respectively. The actual GEONET observed displacement (Fig. 2) need not be considered because this section deals only with the spatial distribution of displacement, not the absolute displacement.

The Y displacement of 4.5 cm was almost half of the MDO, indicating the validity of the method, whereas the value for X was approximately twice that of Y. These results were influenced by the complex scattering properties of man-made objects, and the blurring of

the objects in the range direction. As a result, it is difficult to detect the matching point from slave images. The fairly small standard deviation of 1 to 2 cm (variation of the deviation depending on the slave images) indicates an equal spatial variation for each pair.

4.3 Temporal Features of the Displacement

Figure 6 quantitatively shows that the ratio of data classified as “detect” decreases when the time interval between the image pair increases. Furthermore, a previous study showed that the ratio of “detect” data and the spatial deviation of the displacement have a significant negative correlation in the Y-direction.²³ Therefore, we conducted a temporal analysis of these data to evaluate how the displacement varies when the slave is changed. We utilized the spatial average displacement value in the analysis in order to decrease the effects of matching errors, as the complex scattering of man-made objects is likely to cause geolocation errors.

Table 2 shows the accuracy of the displacement between estimated and GEONET data before correcting for tropospheric delay (TD) (atmospheric interference) and solid Earth tide (SET) (displacement of the land surface by solar and lunar gravity). The accuracy (Ac) was calculated using the time series of the displacement estimated by SAR and the earth motion (EM) calculated by GEONET values as

$$Ac = SAR - EM. \tag{1}$$

Although our evaluation was not strict because the selected matching points and detection rates differed between image pairs, the values were in cross agreement with the displacement accuracy determined in a previous study.¹⁰ Root mean squared error (RMSE) corresponded to about 25% of the pixel spacing (~1.25 m) for X and 6% for Y.

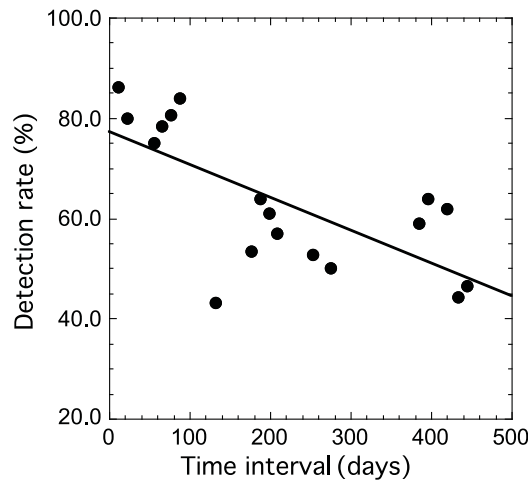


Fig. 6 Relationships between detection rate and time interval. Highly negative correlation was found between them.

Table 2 Accuracy of the displacement from the temporal analysis calculated by comparison with GEONET data.

	X (cm)	Y (cm)
Average	-0.5	-0.6
Maximum	31.0	14.1
Minimum	-34.3	-11.3
RMSE	19.5	7.8

Table 3 Value of estimated displacement SAR, TD, SET, and the EM for each acquired image. Values are normalized by the June 22, 2010, reference date; all measurements in centimeters.

Date	SAR	TD	SET	EM
July 3, 2010	14.3	-0.5	9.1	-0.8
July 14, 2010	46.6	2.8	33.7	-1.6
August 16, 2010	0.8	4.8	-3.8	0.1
August 27, 2010	30.8	0.4	30.2	1.1
September 7, 2010	-6.5	-17.0	25.5	-0.2
September 18, 2010	-13.3	-10.0	1.8	0.6
November 1, 2010	-9.0	-15.1	-2.3	-0.2
December 15, 2010	-38.6	-35.2	11.3	0.0
December 26, 2010	-43.5	-38.3	9.5	-0.1
January 6, 2011	-22.3	-35.4	26.7	1.6
January 17, 2010	-27.3	-40.3	29.4	1.3
March 2, 2011	-7.4	-32.1	27.7	1.0
March 24, 2011	-33.2	-33.7	27.9	-30.9
July 12, 2011	-51.1	-6.7	2.9	-42.1
July 23, 2011	-56.6	-8.7	-0.8	-42.0
August 3, 2011	1.6	5.7	24.5	-42.6
August 25, 2011	-10.2	11.5	-0.5	-44.2
September 5, 2011	-35.2	4.6	-9.0	-47.3

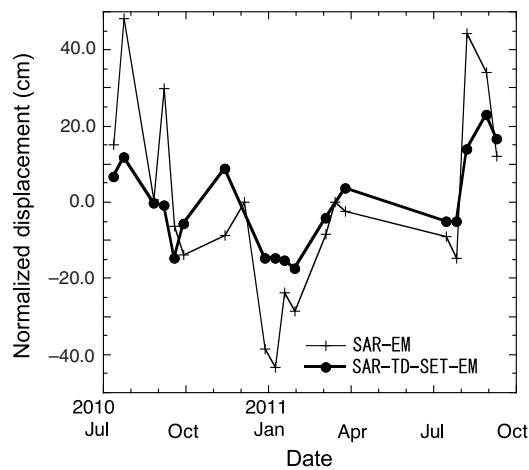


Fig. 7 Normalized displacement calculated from the slant delay first using SAR and earth movement (SAR-EM), then after correction for TD and solid Earth tides (SAR-TD-SET-EM).

5 Discussion

The displacement estimated by SAR is the sum of SET, the EM, and signal propagation delay.²⁴ This delay is incurred in both the troposphere and the ionosphere, though ionospheric delay is

small for the X-band. Overall, TD and SET are the two most important influences on X-band SAR range measurement.¹¹

The troposphere causes signal delay independent of radar frequency; this can be separated into larger hydrostatic (H_D) and smaller wet (W_D) delays.²⁴ For example, the TD for the SR (the direct-line distance between the target and the radar) is calculated as

$$\text{TD} = \frac{H_D + W_D}{\cos \theta}, \quad (2)$$

where θ is the incidence angle of the SR and the altitude. H_D is caused by the presence of dry gases in the atmosphere and can be well-modeled if the atmospheric pressure and altitude are known. W_D is related to precipitation water vapor content. While the magnitude of W_D is generally less than that of H_D , there can be significant temporal variations in W_D . External forces and loading effects deform the solid Earth on different time scales and orders of magnitude. SET is caused by the deformation of the earth due to solar and lunar gravitational forces and can reach up to 40 cm for the radial component and several centimeters for the horizontal components.²⁵

Table 3 shows SAR, TD, SET, and EM at each acquisition date. Values used at each observation date were normalized from a certain reference date of June 22, 2010. All values except TD were recalculated for SR directions by

$$A_{\text{SR}} = \frac{-A_X \cos(\varphi - 90) - A_Y \cos \varphi - A_Z / \cos \theta}{\sin \theta}, \quad (3)$$

where A is the parameter, X , Y , and Z are the components of the parameter, respectively, θ is the incidence angle, and φ is the inclination. The values of H_D and W_D are provided every 3 h at the Kawasaki GEONET ground station, so we obtained the value at 6 AM (JST) on the observation date, while SET was determined at 5:43 AM from the computer program `solid.exe`,²⁶ which calculates the value every minute. The results show that the annual variation in TD and SET is ~ 50 and 40 cm, respectively. The correlation coefficient between SAR and TD was 0.46 though that between SAR and SET was 0.20.

Figure 7 shows the relationships between slant delay calculated only by SAR and EM data (SAR-EM) and that calculated after correcting for TD and SET as well as (SAR-TD-SET-EM). After this correction, the SAR RMSE halves were from 26.0 to 11.9 cm for SR and 8.1 cm for ground range, and it is not related to the time interval. The portion of the residual errors attributable to temporal variation of TD was about 3 cm. The results imply that it is possible to estimate the 2-D displacement within 10 cm after correction for TD and SET.

6 Conclusions

This study evaluated the relative geolocation accuracy of the TerraSAR-X ortho-rectified EEC product by the pixel matching method using 20 pairs of images. Because the chosen study site in urban Tokyo contains many residential and industrial buildings, strong backscattering was easy to extract from the images. Our analysis shows that the spatial deviation of displacement was about 10 cm. This suggests that the 10-cm spatial deviation observed during the GJE, and derived by pixel matching, was significant. On the other hand, the temporal deviation in the estimated displacement was about 20 cm; after removing the effects of TD and SET, this deviation was reduced to ~ 10 cm. The trend of displacement was related to the acquisition season of the slave image positive in the summer and negative in the winter, considering the descending, right-looking orbital direction, as well as the coordinates, the longer slant-range distance corresponded to summer.

In a previous study, the absolute geolocation accuracy of EEC products of TerraSAR-X was evaluated by our team and found to be poorer in mountainous areas due to DEM accuracy.¹⁶ The relative accuracy estimated in our current study quantitatively indicates that geolocation accuracy is independent of DEM errors, however, we need to use geocoded ellipsoid corrected or multilook ground range detected products for more strict analysis. In addition, we suggest

applying the adopted methodology to other cities as well, and performing further quantitative analysis in order to better determine displacement variability.

Acknowledgments

We would like to thank Editage for English language editing.

References

1. D. Tapete et al., "Satellite radar interferometry for monitoring and early-stage warning of structural instability in archaeology sites," *J. Geophys. Eng.* **9**(4), S10–S25 (2012).
2. C. Colesanti et al., "Detection of mining related ground instabilities using the permanent scatterers technique—a case study in the east of France," *Int. J. Remote Sens.* **26**(1), 201–207 (2005).
3. F. Amelung et al., "Sensing the ups and downs of Las Vegas: InSAR reveals structural control of land subsidence and aquifer-system deformation," *Geology* **27**(6), 483–486 (1999).
4. M. Shimada et al., "New global forest/non-forest maps from ALOS PALSAR data (2007–2010)," *Remote Sens. Environ.* **155**, 13–31 (2014).
5. S.-E. Park, Y. Yamaguchi, and D. Kim, "Polarimetric SAR remote sensing of the 2011 Tohoku earthquake using ALOS/PALSAR," *Remote Sens. Environ.* **132**, 212–220 (2013).
6. H. Gokon and S. Koshimura, "Mapping of building damage of the 2011 Tohoku earthquake tsunami in Miyagi prefecture," *Coastal Eng. J.* **54**(1), 1250006 (2012).
7. N. Yague-Martinez et al., "Ground displacement measurement by TerraSAR-X image correlation: the 2011 Tohoku-Oki earthquake," *IEEE Geosci. Remote Sens. Lett.* **9**(4), 539–543 (2012).
8. A. Gabriel, R. Goldstein, and H. Zebker, "Mapping small elevation changes over large areas: differential radar interferometry," *J. Geophys. Res.* **94**(B7), 9183–9191 (1989).
9. W. Liu and F. Yamazaki, "Detection of crustal movement from TerraSAR-X intensity images for the 2011 Tohoku, Japan earthquake," *IEEE Geosci. Remote Sens. Lett.* **10**(1), 199–203 (2013).
10. W. Liu et al., "Estimation of three-dimensional crustal movements in the 2011 Tohoku-Oki, Japan earthquake from TerraSAR-X intensity images," *Nat. Hazards Earth Syst. Sci.* **15**, 637–645 (2015).
11. M. Eineder et al., "Imaging geodesy-toward centimeter-level ranging accuracy with TerraSAR-X," *IEEE Trans. Geosci. Remote Sens.* **49**(2), 661–671 (2011).
12. T. Nonaka and K. Tsukahara, "Application of the geometric accuracy estimation model of the terrain corrected data to TerraSAR-X data," *Shashin Sokuryo to Rimoto Senshingu* **53**(6), 242–249 (2015).
13. T. Fritz and M. Eineder, "TerraSAR-X ground segment, basic product specification document (TX-GS-DD-3302)," p. 126, (2013), <http://sss.terrasar-x.dlr.de/docs/TX-GS-DD-3302.pdf> (20 September 2017).
14. G. Krieger et al., "'TanDEM-X': a satellite formation for high resolution SAR interferometry," *IEEE Trans. Geosci. Remote Sens.* **45**(11), 3317–3341 (2007).
15. GSI, "Fundamental geospatial data (digital elevation model)," <http://fgd.gsi.go.jp/download> (16 March 2017).
16. T. Nonaka et al., "Evaluation of the geometric accuracy of TerraSAR-X," in *Int. Archives of the Photogrammetry, Remote Sensing and Spatial Information Sciences*, Vol. 37, pp. 135–140 (2008).
17. T. Sagiya, "A decade of GEONET: 1994–2003- the continuous GPS observation in Japan and its impact on earthquake studies," *Earth Planet Space* **56**(8), xxix–xli (2004).
18. W. Liu et al., "Detection of three-dimensional geodetic displacements due to the 2011 Tohoku earthquake from TerraSAR-X intensity images," *J. Remote Sens. Soc. Jpn.* **34**(3), 166–176 (2014).
19. M. Tobita et al., "Accurate offset estimation between two SLC images for SAR interferometry," *J. Geod. Soc. Jpn.* **45**(4), 297–314 (1999).

20. T. Hiramatsu and T. Nonaka, "Evaluation of the geometric characteristics for TerraSAR-X multi-temporal images," in *Proc. 53rd Autumn Conf. of the Remote Sensing Society of Japan*, pp. 125–126 (2012).
21. T. Nonaka and T. Hiramatsu, "Mapping displacement around Tokyo International Airport after the Tohoku region pacific coast earthquake 2011 derived from TerraSAR-X imageries," in *Proc. The 4th Asia-Pacific Conf. Synthetic Aperture Radar*, pp. 442–445 (2013).
22. Y. Sakai, S. Koshimura, and M. Matsuoka, "Estimation of tsunami-induced building damage using TerraSAR-X intensity images," *J. Jpn. Soc. Civil Eng.* **69**(2), I_1456–I_1460 (2013).
23. T. Nonaka, T. Asaka, and K. Iwashita, "Evaluation of relative geometric accuracy of TerraSAR-X by pixel matching methodology," in *Int. Archives of the Photogrammetry, Remote Sensing & Spatial Information Science*, Vol. 41, No. B7, pp. 859–864 (2016).
24. R. Hanssen, *Radar Interferometry—Data Interpretation and Error Analysis*, p. 308, Springer, Netherlands (2001).
25. K. Lambeck, *Geophysical Geodesy: The Slow Deformations of the Earth*, Oxford Science Publications, Oxford University Press, Oxford, United Kingdom (1988).
26. D. Milbert, "Solid.exe program," <http://geodesyworld.github.io/SOFTS/solid.htm> (16 March 2017).

Takashi Nonaka received his PhD in engineering from Tokyo Institute of Technology in 2004. After working for PASCO Corporation for 11 years, he joined Nihon University in 2015. He is an associate professor at Nihon University. One of his main research interests is the application of the high-resolution commercial SAR satellite data, especially for disaster monitoring.

Tomohito Asaka received his PhD in engineering from Nihon University in 2007. He is an assistant professor at the College of Industrial Technology, Nihon University. He teaches basic structural dynamics, surveying practice, applied surveying, and remote sensing in the Department of Civil Engineering. He also has been active in a collaborative research of JAXA using ALOS-2/PALSAR-2 as a principal investigator (No. 3099) since 2016.

Keishi Iwashita received his double PhD from the Graduate School of Arts and Science, New York University, in 1998, and Nihon University in 2009, respectively. He has been on the Nihon University faculty since 1983. He has had a certified fellowship and has been a temporary faculty member of the University of California, Los Angeles, Image Mapping Lab, since 2001. In the remote sensing field, he specializes in optics, radiative transfer, and ocean color remote sensing.

Wen Liu received her PhD in engineering from Chiba University in 2013. She joined Chiba University in 2014 as an assistant professor. Her research interest is in urban remote sensing using very-high-resolution optical sensors and synthetic aperture radars.

Fumio Yamazaki received his PhD in civil engineering from the University of Tokyo in 1987. He joined the University of Tokyo in 1989 as an associate professor. He joined Chiba University as a professor in 2003. His research interests include earthquake engineering, stochastic mechanics, and the application of GIS and remote sensing to disaster management.

Tadashi Sasagawa received his PhD in engineering from Hokkaido University in 2005. He is an executive technical advisor of PASCO Corporation. From 2006 to 2013, he served as a part-time lecturer at the University of Tokyo. He led the introduction of aircraft sensors, digital photogrammetry, and remote sensing with TerraSAR-X images in Japan.